AN INVESTIGATION OF THE EFFECT OF SST MESOSCALE VARIABILITY ON THE DYNAMICS OF THE NORTH PACIFIC JET STREAM AND STORM TRACK

A Thesis

by

ERIC MATTHEW FORINASH

Submitted to the Office of Graduate and Professional Studies of
Texas A&M University
in partial fulfillment of the requirements for the degree of

MASTER OF SCIENCE

Chair of Committee,	Istvan Szunyogh
Committee Members,	Craig Epifanio
	Ping Chang
Head of Department,	Ramalingam Saravanan

December 2019

Major Subject: Atmospheric Sciences

ABSTRACT

The effect of SST mesoscale variability on the dynamics of the North Pacific Jet Stream and Storm track is investigated based on simulations with a global atmospheric circulation model coupled to a slab ocean model. The investigation is carried out by comparing time- and ensemble-averaged terms of the atmospheric eddy kinetic energy for two ensembles. The difference between the two ensembles is that SST mesoscale variability is retained in only one of them. It is found that SST mesoscale variability has a major effect on both the baroclinic and barotropic energy conversion processes in the atmosphere. For the investigated two-week period in the North Pacific, the net effect of the changes in the energy conversion processes on the jet stream is similar to that of a drag force. In addition, baroclinic energy conversion is suppressed and the eddy kinetic energy is reduced along the storm track.

ACKNOWLEDGEMENTS

I would like to thank my committee chair and advisor, Dr. Szunyogh, and my committee members, Dr. Epifanio, and Dr. Chang, for their continued guidance and support throughout my academic career and research.

Huge thanks to all my friends, professors, and colleagues for making my time here at Texas A&M University a wonderful and priceless experience.

CONTRIBUTORS AND FUNDING SOURCES

Contributors

This work was supervised by a thesis committee consisting of Professor Istvan Szunyogh (advisor) and Professor Craig Epifanio of the Department of Atmospheric Sciences and Professor Ping Chang of the Department of Oceanography.

The data analyzed for the results was provided by Yinglai Jai and further advanced by Gyorgyi Gyarmati. The SST field in Figure 2 was produced and provided by Yinglai Jai. A modified version of the FORTRAN code made by Michael Herrera was used in computing the terms and output files associated with the results.

All other work conducted for the thesis was completed by the student independently. The thesis is based on parts of the manuscript "An Investigation of the Effect of SST Mesoscale Variability on the Dynamics of the North Pacific Jet Stream and Storm Track" by I. Szunyogh, E. Forinash, G. Gyarmati, Y. Jia, P. Chang, and R. Saravanan, to be submitted to the Journal of Geophysical Research-Atmosphere.

Funding Sources

This research has been conducted as part of the NOAA MAPP S2S Prediction Task Force and supported by NOAA grant NA16OAR4311082. The data used for the preparation of the figures is publicly available at https://doi.pangaea.de/10.1594/PANGAEA.897395.

TABLE OF CONTENTS

LIST OF FIGURES

1. INTRODUCTION

It has been shown that large-scale oceanic fronts, such as the Kuroshio Extension or the Gulf Stream, play an important role in the dynamics of the midlatitude atmospheric storm tracks [*Nakamura* et al. 2004, *Nakamura* et al. 2008]. *Dickson* and *Namias* [1976] and *Gulev et al.* [2003] concluded that the significant temperature gradient between a cool landmass and a warmer boundary current like the Kuroshio impacts the activity over the midlatitude storm tracks in winter. In addition, the increase in moisture and heat fluxes over the Kuroshio has also been known to aid in the development of cyclogenesis and therefore storm track formation [*Hoskins and Valdes* 1990]. It is also well understood that SST anomalies associated with the ocean mesoscale eddies that develop along those oceanic fronts have a major effect on the atmospheric boundary layer [*Chelton and Xie* 2010; *Chelton* et al. 2004; *Small* 2008; *Xie* 2004]. The impact of the mesoscale SST anomalies on the dynamics of the jet streams and the storms tracks in the upper troposphere is far less understood and has been investigated only by a handful of studies [e.g., *Foussard et al.* 2019]. *Foussard et al.* [2019] concluded based on numerical solutions using the Weather Research and Forecasting (WRF) model that when ocean eddies are taken into account, there is a poleward shift of both the jet and the storm track. Large-scale downstream responses from eddy driven SST anomalies have also been known to impact the jet position and weather patterns across the Pacific, Atlantic, and Southern Ocean [*Frankignoul et al.* 2011; *O'Reily and Czaja* 2015]. One of the first studies that investigated the effect of mesoscale SST variability on the North Atlantic storm track was *Woollings et al.* [2010]. That study carried out numerical experiments with a 0.44°-resolution, limited area version of the Hadley Centre's third generation atmospheric model and found that mesoscale SST variability had a subtle, but significant effect on the storm track. *Ma et al.* [2015, 2017] carried out atmospheric simulations

with the limited WRF model at a horizontal resolution of 27 km for the North Pacific. In their study, one set of simulations was forced by 0.09°-resolution SST analyses, which resolved mesoscale SST variability along the Kuroshio Extension, while the other set of simulations was carried out by suppressing the mesoscale SST variability by spatial filtering. They found that mesoscale SST variability had a deep tropospheric impact that extended along the North Pacific storm track, down to the west coast of North America at the eastern lateral boundary of the model domain. *Foussard et al.* [2019] carried out idealized midlatitude channel model experiments with the WRF model at horizontal resolution of 18 km with 50 model levels. They investigated the effects of the SST footprint of localized eddies added to a large-scale zonally symmetric large-scale atmospheric front. They found that the eddies pushed the jet stream and the storm track poleward. *Herrera et al.* [2015] found that nearly all global ensemble forecast systems predicted the slowly varying large-scale component of the atmospheric flow with a systematic error whose magnitude increased with the forecast time. Misrepresentation of the atmosphere-ocean interactions in the models can be one of the potential sources of such an error. Our goal is to investigate the possibility that ocean mesoscale eddy-atmosphere (OME-A) feedback is such a process. Because ocean mesoscale eddies persist for months, they may play an important role in S2S predictability through modulating the storm tracks.

The present study builds on the numerical experiments of *Jia et al.* [2019] that were carried out with a configuration of the Community Earth System Model (CESM) of the National Center for Atmospheric Research (NCAR), in which the global atmospheric model was thermodynamically coupled to a slab ocean model. The experiments were carried out at horizontal resolution 0.23° times 0.23° with 30 vertical model levels. They showed, in good agreement with *Ma et al.* [2015, 2017] and *Foussard et al.* [2019], that the mesoscale SST

anomalies enhanced the moisture fluxes in the lower troposphere in the midlatitudes. An examination of the variance of the meridional component of the wind at the jet level suggested that the mesoscale SST anomalies increased the intensity of the midlatitude storm tracks. It was hypothesized that this intensification may have been the result of the enhanced moisture fluxes leading to more intense baroclinic energy conversion in the entrance regions of the storm tracks. A more surprising result was the weakening of the North Pacific jet stream by about 10%. It was speculated that the vertical atmospheric motions induced by ocean mesoscale variability may have excited vertically propagating gravity waves that led to a gravity wave drag on the large-scale atmospheric flow. Our goal is to further examine the hypotheses of *Jia et al.* [2019] with the help of the eddy kinetic energy equation.

2. BACKGROUND

2.1. The Coupled Model

Jia et al. [2019] generated two ensembles of model simulations that were forced by daily 0000 UTC NOAA Optimum Interpolation Sea Surface Temperature and ICE (OISSTV2) analyses data from December 2007. That particular month was chosen, because it was the time of an unstable epoch of the Kuroshio Extension that produced active mesoscale ocean eddies and strong mesoscale SST anomalies, but was also a time when the El Nino-Southern Oscillation (ENSO) and the Pacific Decadal Oscillation (PDO) were nearly neutral. It was also the period investigated by *Ma et al.* [2015, 2017]. The two ensembles differed in the treatment of the SST data. Unlike in an uncoupled atmospheric simulation, in a coupled slab ocean simulation, the input SST data is used directly only to define the initial condition of the slab ocean model that has the single prognostic equation

$$\frac{\partial T_{mixed}}{\partial t}(\boldsymbol{r},t) = \frac{1}{\rho c_0 h_{mixed}(\boldsymbol{r})}[Q_{atm}(\boldsymbol{r},t) - Q_{ocn}(\boldsymbol{r},t)], \quad (1)$$

where **r** is the two-dimensional vector of horizontal location, *t* is time, $T_{mixed}(\mathbf{r},t)$ is the SST, ρ is the density of the ocean water, c_0 is the specific heat of the ocean water, $h_{mixed}(\mathbf{r})$ is the depth of the ocean mixed layer, $Q_{atm}(\mathbf{r},t)$ is the net heat transfer from the atmosphere to the mixed layer, and $Q_{ocn}(\mathbf{r},t)$ is the net (horizontal and vertical) heat transfer to other parts of the ocean. In the experiments of *Jia et al.* [2019], the constants of Eq. (1) were taken to be rho = 1026 kgm^{-3} and c_0 = 3930 Jkg^{-1} K^{-1}, and $h_{mixed}(r)$ is determined from the *Levitus* [1982] Climatological Atlas of the World Ocean.

The field $Q_{ocn}(\mathbf{r},t)$ is a prescribed input field in a slab ocean model, in which it represents the thermodynamical effects of the internal ocean dynamics. *Jia et al.* [2019] obtained the

estimate of $Q_{ocn}(\mathbf{r},t)$ used in the coupled slab ocean model experiments by first computing an estimate of

$$Q_{atm}(\boldsymbol{r},t) = Q_{sol}(\boldsymbol{r},t) - Q_{long}(\boldsymbol{r},t) - Q_{sen} - Q_{latent}(\boldsymbol{r},t), \quad (2)$$

for December 2007 from an ensemble of uncoupled atmospheric model simulations. In Eq. (2), Q_{sol} is the net radiative heating of the ocean mixed layer by solar radiation, Q_{long} is the net long-wave radiative cooling of the ocean mixed later, Q_{sen} is the net sensible heat flux from the ocean to the atmosphere, and Q_{latent} is the net latent heat flux from the ocean to the atmosphere. The members of the ensemble of atmospheric simulations started from different atmospheric initial conditions but used the same time series of observation-based SST analyses from December 2007 to compute the thermal forcing by the ocean. $Q_{ocn}(\mathbf{r},t)$ was then computed for each ensemble member from Eq. (1), by using the SST analyses to approximate the left-hand side of the equation by finite differences. Next, these estimates were then averaged over the respective ensemble and time for the entire month to obtain $\bar{Q}_{ocn}(\mathbf{r})$. This time independent field was then used to define $Q_{ocn}(\mathbf{r},t)$ ($Q_{ocn}(\mathbf{r},t) = \bar{Q}_{ocn}(\mathbf{r})$) in the single prognostic equation of the slab ocean model of the coupled experiments. This specific design all the SST to change in response to the changes in $Q_{atm}(\mathbf{r},t)$, which leads to a nonlinear feedback mechanism between the atmosphere and the ocean. Interestingly, *Jia et al.* [2019] observed a chaotic divergence of the SST between the ensemble members.

A key difference between the coupled experiments of *Jia et al.* [2019] and the non-coupled experiments of *Woollings et al.* [2010], *Ma et al.* [2015, 2017], and *Foussard et al.* [2019] is that in the coupled experiment, the transfer of internal energy from the ocean to the atmosphere in the form of heat reduces the SST. This is a potentially crucial difference, because

Woollings et al. [2010] and *Foussard et al.* [2019] found that the ocean eddies affected the storm track by increasing the intensity and shifting the location of diabatic heating.

2.2. The Control and Filtered Ensemble

The two ensembles of *Jia et al.* [2019] differed in the treatment of the input SST data. One used the original 0.23° x 0.23° SST data for the estimation of $\bar{Q}_{ocn}$**(r)** and the definition of the SST initial condition at 0000 UTC, 1 December, 2007, while the other used the SST data for both purposes after filtering the mesoscale variability by a 5° x 5° boxcar filter. Each ensemble had 30 members, which were started from a set of 30 atmospheric initial conditions that was identical for the two ensembles. These atmospheric initial conditions were generated by an integration of the atmospheric model from 0000 UTC 15 November, 2007 to 2400 UTC 30 December, 2007, using a climatological mean state as atmospheric initial condition, and then changing the dates associated with the 0000 UTC atmospheric states from the last 30 days of the simulation to 0000 UTC 1 December, 2007. Differences in the atmospheric state and the SST between the two ensembles developed in response to the differences between the SST initial condition at 0000 UTC, 1 December, 2007 and the Q_{ocn}(r,t) fields for the month of December, 2007, while differences within the ensembles developed in response to the differences between the atmospheric initial conditions.

Following the terminology of *Jia et al.* [2019], we call the ensemble with mesoscale SST variability the *control ensemble*, and the other ensemble the *filtered ensemble*. We compare ensemble-mean diagnostics for the two ensembles to examine the effect of mesoscale SST variability on the energy conversion and transport processes in the troposphere. These ensemble-mean diagnostics are obtained by computing the ensemble mean of the time-averaged diagnostics for weeks 3 and 4 of the simulations based on 6-hourly model output. To save

computational time, the diagnostics are computed for 15 of the 30 ensemble members of *Jia et al.* [2019]. To verify that the reduction of the number of ensemble members has no major effect on the results, we reproduced the result of *Jia et al.* [2019] for the 15-member ensemble (results not shown) before the calculation of our diagnostics. We found no qualitative differences and only minor quantitative differences between the 15 and 30-member ensembles means.

2.3. The Eddy Kinetic Energy Equation

The eddy kinetic energy of *Orlanski and Katzfey* [1991] and *Orlanski et al.* [1995] is based on decomposing the atmospheric state variables into a time-mean and an eddy (transient) component. It was originally introduced to investigate the energy transport and conversion processes in individual weather events and has played an important role in developing our current understanding of storm track dynamics [e.g., *Chang and Orlanski,* 1993, 2005]. Formally, the equation is

$$\frac{\partial}{\partial t}\langle K_e\rangle = \overbrace{-\langle\nabla\cdot\mathbf{v}K_e\rangle}^{1}\overbrace{-\langle\nabla\cdot\mathbf{v}'\phi'\rangle}^{2}\overbrace{-\langle\omega'\alpha'\rangle}^{3}\overbrace{-\langle\mathbf{v}'\cdot(\mathbf{v}_3'\cdot\nabla_3)\,\overline{\mathbf{v}}-\mathbf{v}'\cdot\overline{(\mathbf{v}_3'\cdot\nabla_3)\,\mathbf{v}'}\rangle}^{4}$$
$$\overbrace{-\langle\nabla_p\cdot\omega'K_e\rangle}^{5}\overbrace{-\langle\nabla_p\cdot\omega'\phi'\rangle}^{6}\overbrace{+\langle(\mathrm{Residue})\rangle}^{7}, \tag{3}$$

where the argument (r,t) is not included in the notation of state variables for the sake of brevity. The equation is written using the pressure p as the vertical coordinate of the vector of position r. The angle bracket stands for the vertical mean

$$\langle A\rangle = \frac{1}{(p_t - p_b)}\int_{t_b}^{p_t} A\,dp$$

of an arbitrary scalar A for the layer between pressure levels pb and pt. In our diagnostic calculations, $p_b = p_s(\mathrm{r,t})$, where $p_s(\mathrm{r,t})$ is the surface pressure and $p_t = 100\ hPa$. (The contribution of the different processes at the different vertical levels can be investigated be examining the

vertical profiles of the integrand A(p) for the different terms.) The prime indicates the eddy component of a variable, while the bar indicates a time averaged term. (In our calculations, all time-means are computed for weeks 3 and 4 of the simulations.) The state variables in the equation are the wind vector $v_3 = (v,p)$, $v = (u,v)$, where u is the zonal and v the meridional component of the wind vector; $K_e = (u'^2 + v'^2)/2$ is the eddy kinetic energy density, φ is the geopotential, $\omega = dp/dt$ is the vertical velocity, and α is the specific volume. The spatial derivatives are represented by the del operator: $\nabla_3 = (\nabla, \partial/\partial p)$, $\nabla = (\partial/\partial x, \partial/\partial y)$, while the dot indicates the scalar product of two vectors.

Terms 1 (horizontal eddy kinetic energy transport) and 2 (ageostrophic geopotential flux convergence) are transport terms that cannot be global sources or sinks of the eddy kinetic energy (their global integral for the atmosphere is zero). Term 1 is negative when more potential eddy kinetic energy to be removed from a location and positive when eddy kinetic energy is being supplied to the location. *Szunyogh* [2014] describes term 2 as

$$-\nabla_H \cdot \mathbf{v}'_H \phi' = -\nabla_H \cdot \mathbf{v}'_{af0} \phi'$$

which states at the reference latitude, the geopotential flux convergence is only impacted by the ageostrophic component of the horizontal wind. Analysis typically focuses on the local energetics within a narrow latitude band, where it is known that the Coriolis parameter changes are negligible and therefore the geopotential flux convergence is dominated by the ageostrophic component of the horizontal wind perturbation [*Szunyogh*, 2014]. Terms 5 and 6 are the related vertical transport terms. While these terms are not zero, because of the possible transport of K_e and f through the bottom and top of the atmospheric layer, they are orders of magnitude smaller than the dominant terms and can be neglected. Term 5 and 6 are still computed and showed in

our results to confirm that their magnitudes are significantly smaller than the first four terms of the Eddy Kinetic Energy Equation and therefore can be neglected; they are also included in our total residual calculation. Term 3 is the baroclinic energy conversion term and is almost always positive in the terrestrial atmosphere, indicating rising warm air and sinking cold air. It is always important to verify, however, that a positive value of $-\omega'\alpha'$ (vertical temperature flux) is accompanied by a positive value of the meridional temperature flux, $-v'T'$ to confirm that the vertical motions are associated with baroclinic instability rather than convection. Term 4 is the sum of two terms, of which the first is always the dominant one. Because this term describes the transfer of kinetic energy from the time mean flow to the eddies, it is called the barotropic energy conversion term. A negative value of this term indicates that kinetic energy is transferred from the eddies to the mean flow; whereas a positive value of this term indicates that kinetic energy is transferred from the mean flow to the atmospheric eddies component. Term 7 is the residue term that can be calculated by computing the difference between the left-hand side of the equation and the sum of the other terms of the right-hand side of the equation. It represents the effects of the processes not resolved by the estimates of the other terms. Because the most important such process is dissipation of the eddy kinetic energy, this term is typically negative. The residue term, however, is also affected by the errors of the approximations made to compute the other terms of the equation. In our calculations, these errors include the truncation errors of the finite difference schemes used for the approximation of the spatial derivatives and the sampling errors associated with using fields for the computations that are 6 h apart.

We compute the terms of Eq. (3) for each ensemble members every 6 h, then the time-mean of the terms, and finally the ensemble-mean of the terms separately for two ensembles

(control and filtered). For the computation of the time mean of the left-hand side of Eq. (3), which we use for the computation of the time-mean of the residue term, we take advantage of

$$\overline{\frac{\partial}{\partial t}\langle K_e\rangle} = \frac{1}{T}\int_{t_0}^{t_0+T}\frac{\partial}{\partial t}\langle K_e\rangle dt = \frac{1}{T}[\langle K_e\rangle(t_0+T) - \langle K_e\rangle(t_0)], \tag{4}$$

where T is 2 weeks. For the computation of the time-mean of the terms of the right-hand side, we use the approximation

$$\overline{\frac{\partial}{\partial t}\langle A\rangle} = \frac{1}{T}\int_{t_0}^{t_0+T}\langle A\rangle dt \approx \frac{1}{N\Delta T}\sum_{i=0}^{N} A_i\Delta T = \frac{1}{N}\sum_{i=0}^{N} A_i, \tag{5}$$

where N = 56 is the number of 6-hour time intervals ΔT that span T. As already mentioned, terms 5, 6, and the second part of Term 4 are negligible even before taking the time and ensemble mean. *Chang and Orlanski* [1993] found that where the baroclinic conversion process had a maximum downstream of the source that enhances baroclinicity, eddies formed and were sustained further downstream despite the lower values of baroclinicity. In addition, while Term 2 plays an important role in storm track dynamics [e.g., *Chang and Orlanski,* 1993; *Chang*, 1993], its time and ensemble average insignificant. Hence,

$$\overline{\frac{\partial}{\partial t}\langle K_e\rangle} \approx \overbrace{-\overline{\langle\nabla\cdot\mathbf{v}K_e\rangle}}^{1}\overbrace{-\overline{\langle\omega'\alpha'\rangle}}^{3}\overbrace{-\overline{\langle\mathbf{v}'\cdot(\mathbf{v}'_3\cdot\nabla_3)\,\overline{\mathbf{v}}\rangle}}^{4}\overbrace{+\langle(\text{Residue})\rangle}^{7}, \tag{6}$$

is a highly accurate and useful approximation to formulate arguments about the roles of the different physical processes. (Notice the no additional notation was introduced to indicate ensemble averaging, even though it is always done in our calculations, to avoid further

complicating the notations.) Some care has to be taken, however, analyzing the vertical cross sections of the integrands, because in that case, the integrand of Term 5, $\nabla_p \cdot \omega' K_e$, must also been considered: while the vertical transport of kinetic energy does not change the mean eddy kinetic energy in the atmospheric column, it plays an important role in the vertical rearrangement of the eddy kinetic energy in the column.

3. RESULTS

3.1. Oceanic Heat Transfer

Investigating the differences between the $\bar{Q}_{\text{ocn}}(\mathbf{r})$ fields of the two experiments provides important information about the effect of SST mesoscale variability on the atmospheric heat transport. In essence, $\bar{Q}_{\text{ocn}}(\mathbf{r})$ is a measure of the part of the temporal changes of the SST that cannot be explained by the transfer of heat from the ocean to the atmosphere. At locations where $\bar{Q}_{\text{ocn}}(\mathbf{r})$ is positive, the ocean transports heat from that location to the mixed layer, while at locations where $\bar{Q}_{\text{ocn}}(\mathbf{r})$ is negative, the ocean transports heat to that location from the mixed layer (Fig. 1, modified from *Jia et al.* [2019]). Most significantly, sharp boundaries between regions of positive and negative values in the difference field (bottom panel) indicate locations where ocean mesoscale variability is present and therefore leads to oceanic heat transport from the region of positive values to the region of negative values. One of the clearest examples occurs over the North Pacific along the Kuroshio Extension, in which case the mesoscale eddies are marked by mesoscale patterns of alternating negative and positive values along the green line segment.

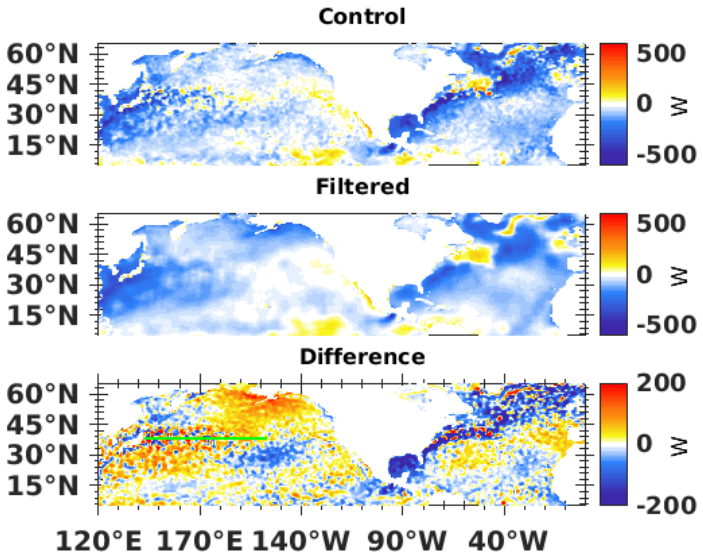

Figure 1. Illustration of the differences between the prescribed ocean heat transport fields of the two experiments. Shown is (color shades) $\overline{\boldsymbol{Q}}_{\mathbf{ocn}}(\mathbf{r})$ for (top) the control experiment and (middle) the filtered experiment. Also shown (bottom) is the difference between the $\overline{\boldsymbol{Q}}_{\mathbf{ocn}}(\mathbf{r})$ fields of the two experiments. The green line segment in the North Pacific along the 38°N indicates the location of the vertical cross-sections of section 3.4. Modified from *Jia et al.* [2019].

Over the Kuroshio Extension, the thermal signature of the mesoscale eddies is stronger but the divide between the region of positive values to the south and the region of negative values to the north is less pronounced as compared to the North Atlantic Gulf Stream. Another interesting feature of the $\overline{Q}_{\mathrm{ocn}}(\mathbf{r})$ difference field in the North Pacific is the large-scale pattern of positive values in the Gulf of Alaska and the somewhat smaller pattern of negative values to the south of that region (south-east of the Kuroshio Extension). We interpret that these patterns are closely related to the strong large-scale atmospheric response in those regions to the presence of SST mesoscale variability. However, part of this response may be an artifact of the approach used for the estimation of the oceanic heat transport: because the circulation of $\overline{Q}_{\mathrm{ocn}}(\mathbf{r})$ does not account for the atmospheric feedback to the SST, the effect of that feedback must be absorbed in $\overline{Q}_{\mathrm{ocn}}(\mathbf{r})$. Therefore, if the atmospheric response and resulting feedback to the ocean were stronger in the simulations that were used for the estimation of $\overline{Q}_{\mathrm{ocn}}(\mathbf{r})$ of the control experiment, the bias

introduced into the estimate must have been stronger. We can investigate this possibility by inspecting Figure 1 of *Jia et al.* [2019], which represents the geographic distribution of the SST bias of the two experiments. We find that while there is a weak cold SST bias in the control experiment in part of the Gulf of Alaska, the size of the region of negative bias is much smaller than the pattern of positive $\bar{Q}_{\mathrm{ocn}}(\mathbf{r})$ difference, and the bias in the region to the south is weaker in the control experiment.

3.2. SST and the Atmospheric Mean Flow

We begin the investigation of the link between mesoscale SST variability and atmospheric dynamics by first examining the relationship between the atmospheric mean flow and the mean SST field for the control and filtered ensemble (Fig. 2). The color scheme of the figures that show the SST fields is specifically chosen such that white color outlines the approximate position of the Kuroshio Extension and its eastward propagation, the North Pacific Current, and the eastward flowing northern segment of the Gulf Stream and its extension, and the North Atlantic Current. The SST indication of mesoscale ocean eddies are clearly visible looking at the control experiment (top panel), but are absent in the filtered experiment (middle panel). The SST difference field (bottom panel) distinctly shows the positive and negative anomalies located in the Kuroshio Extension region that are associated with mesoscale ocean eddies in the control experiment. Since mesoscale ocean eddies are highly persistent features of the oceanic flow, time and ensemble averaging do not filter the eddies [e.g. *Chelton et al*., 2004]. While in other parts of the North Pacific outside of the Kuroshio Extension region also consists of mesoscale structures, the mesoscale structures are organized into larger scale patterns of positive and negative anomalies.

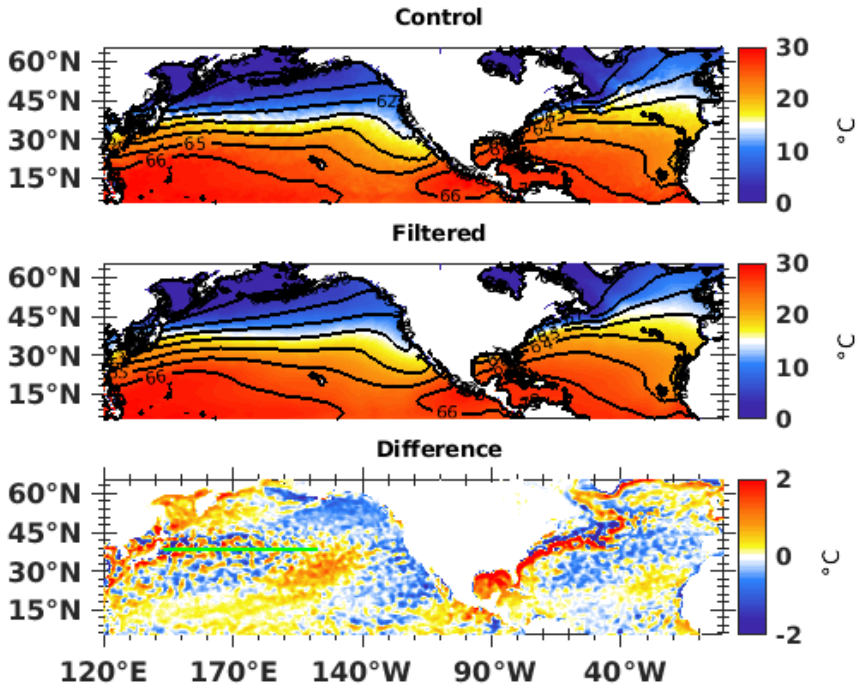

Figure 2. Geographical distribution of the mean SST for the experiments. Shown are (color shades) the SST and (contours) the mean geopotential height at 992 hPa for (top) the control experiment and (middle) the filtered experiment. Also shown are (bottom) the differences between the fields of the top two panels. The green line segment in the North Pacific along 38°N indicates the location of the vertical cross-sections of section 3.3.

At locations where the SST is higher, the time-mean geopotential height of the constant pressure surfaces close to the bottom of the atmosphere also tends to be greater (top two panels of Fig. 2). This direct relationship between the low-level atmospheric flow and the SST suggests that the low-level atmospheric mean flow is controlled by the SST. This process can be explained through the simple thermodynamical argument that over warmer sea surfaces, the higher temperature of air forces the constant pressure surfaces to rise by the vertical expansion of the atmospheric air column. This same effect also helps explain the close relationship between the low-level geopotential height differences (bottom panel of Fig. 3) and the SST: in regions of positive (negative) SST differences, the geopotential height difference is also positive (negative). While the geopotential height differences become deeper higher up in the troposphere (middle and top panel of Fig. 3), where other dynamical processes modulate their spatial structure, their

correlation with the patterns of low-level geopotential height and SST differences remains clear. For example, the relative trough just off the Pacific Coast of North America has its roots in negative SST anomalies, and the relative ridge to the west of the relative trough is related to positive SST anomalies west of the region of negative SST anomalies.

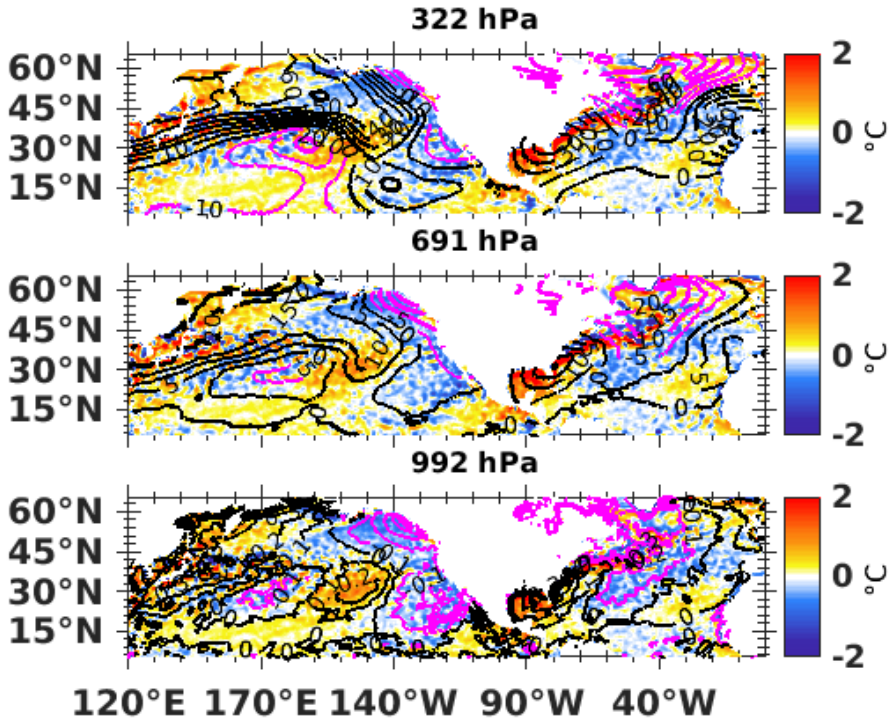

Figure 3. Illustration of the effect of SST differences on the vertical structure of the atmospheric mean flow. Shown are (color shades) the SST and (contours) the mean geopotential height difference at (bottom) 992 hPa, (middle) 691 hPa, and (top) 322 hPa. Black contours indicate positive, while magenta contours indicate negative values. The contour intervals are 0.2 gpm, 5 gpm, and 10 gpm at 992 hPa, 691 hPa, and 322 hPa, respectively.

In the Kuroshio Extension region, where there are no larger scale SST difference patterns, the mesoscale SST anomalies have a major impact on the jet stream (top panel of Fig. 3). From *Jia et al.* [2019] we know that this difference is a weakening of the North Pacific Jet by about 10% by the ocean mesoscale eddies in the control experiments. This weakening of the North Pacific Jet is the main subject of our investigation presented in sections 3.2 and 3.3.

Regarding this result, we point out that the changes in the jet and the relative ridge over the North-east Pacific are clearly connected (top panel of Fig. 3).

3.3. Geographical Maps of the Energetics

We focus our attention over the Pacific and Atlantic Ocean in our studies, especially over the Kuroshio region, with figure axis' ranging from 5° - 65° latitude North and 120°E to 0° longitude. Figure 4 shows the geographical distribution of the mean eddy kinetic energy from 5° - 65° latitude North and 120°E to 0° longitude. The North Pacific storm track and the North Atlantic storm track are the two regions of high eddy kinetic energy that are connected over North America. In the entrance region of the North Pacific storm track, off the coast of Japan, and to the east along the North Pacific jet, the eddy kinetic energy is lower in the control experiment than in the filtered experiment. The geopotential height difference field indicates that the reduction of the eddy kinetic energy is associated with a weaker jet and a relative ridge in the exit region of the jet. To the east of the relative ridge, there is a relative trough in the control experiment that is also a region of increased eddy kinetic energy. This pattern of increased eddy kinetic energy extends far into the east, following the regions of negative geopotential height differences, all the way to the exist region of the North Atlantic storm track. The extension of the pattern of increased eddy kinetic energy to the west is to the north of the North Pacific storm track.

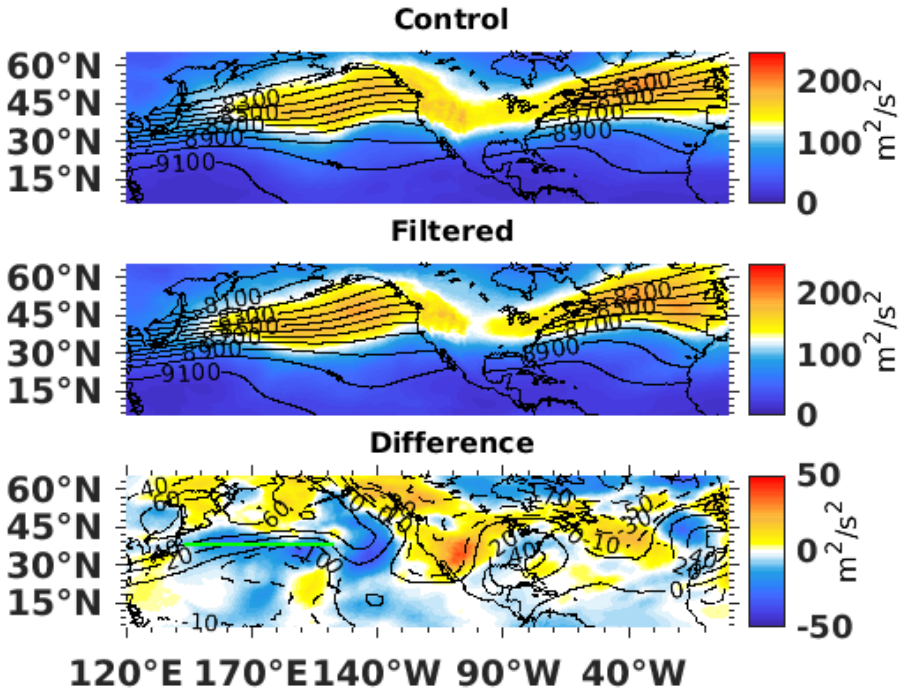

Figure 4. Geographical distribution of the eddy kinetic energy in the experiments. Shown are (color shades) $\overline{< \boldsymbol{Ke} >}$ and (contours) the time- and ensemble-average geopotential height at 322 hPa for (top) the control experiment and (middle) the filtered experiment. Also shown are (bottom) the differences between the fields of the top two panels. The green line segment in the North Pacific along 38°N indicates the location of the vertical cross-sections of section 3.3.

The main source of the eddy kinetic energy of the extratropical storm track is baroclinic energy conversion. The intensity of this process is reduced along the North Pacific storm track and increased along the North Atlantic storm track in the presence of mesoscale SST variability (Fig. 5). These changes in the intensity of the baroclinic energy conversion are consistent with the respective decrease and increase of the eddy kinetic energy of the two storm tracks in the control experiment. Another energetics process that could potentially contribute to the lower level of eddy kinetic energy of the North Pacific storm track is the horizontal transport of eddy

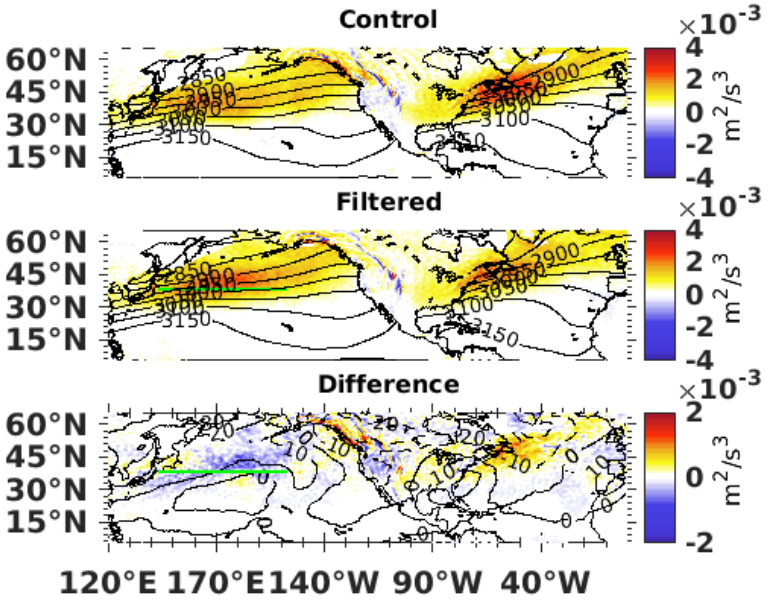

Figure 5. Geographical distribution of the baroclinic energy conversion in the experiments. Shown are (color shades) $-\overline{<\boldsymbol{\omega}'\boldsymbol{\alpha}'>}$ for the locations where $\boldsymbol{\nu}'\boldsymbol{T}' > \mathbf{0}$ and (contours) the time- and ensemble-average geopotential height at 691 hPa for (top) the control experiment and (middle) the filtered experiment. Also shown are (bottom) the differences between the fields of the top two panels. The green line segment in the North Pacific along 38°N indicates the location of the vertical cross-sections of section 3.3.

kinetic energy: because the net horizontal eddy kinetic energy is negative (transported out) in the main regions of baroclinic energy conversion (Fig. 6), a larger net loss (more intense transport) in the control experiment could also contribute as an additional source to the reduction of the eddy kinetic energy in the upstream part of the North Pacific storm track. But, this is not the case, as the difference between the transport terms of the two experiments is positive (Figure 6, bottom panel), which indicates that less eddy kinetic energy is transported out from the main region of baroclinic energy production in the North Pacific storm track in the control experiment. In other words, the reduced downstream transport of eddy kinetic energy is led by the reduced production of eddy kinetic energy by baroclinic energy conversion. As expected, the magnitude

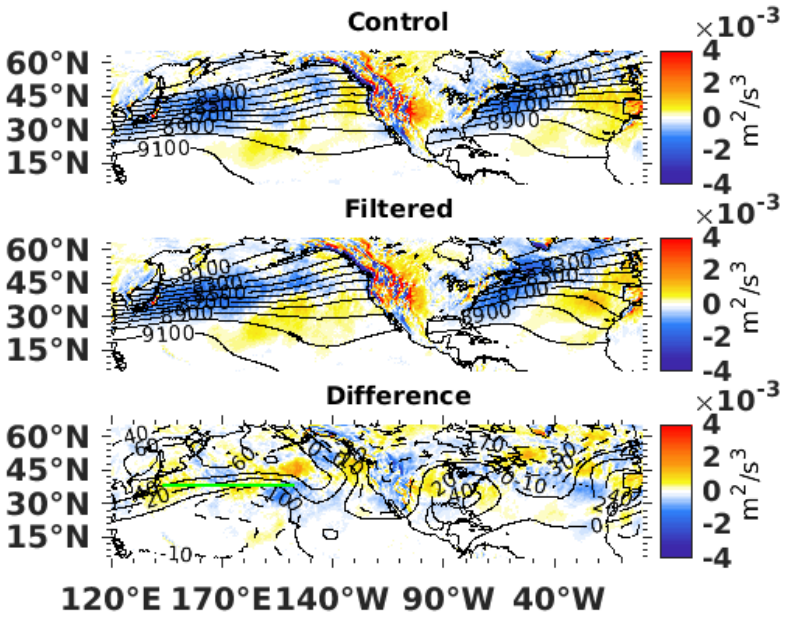

Figure 6. Geographical distribution of the horizontal eddy kinetic energy transport in the experiments. Shown are (color shades) $-\overline{\langle \boldsymbol{\nabla} \cdot \boldsymbol{vKe} \rangle}$ and (contours) the time- and ensemble-average geopotential height at 322 hPa for (top) the control experiment and (middle) the filtered experiment. Also shown are (bottom) the differences between the fields of the top two panels. The green line segment in the North Pacific along 38°N indicates the location of the vertical cross-sections of section 3.3.

of the ageostrophic geopotential flux convergence, the other horizontal transport term, is much smaller than that of the horizontal eddy kinetic energy transport or the baroclinic energy conversion in both experiments (Fig. 7). However, the magnitude of the difference between the fields in the two experiments is non-negligible in the regions of relative trough and ridges in the mean flow. Most importantly, the mean ageostrophic geopotential flux convergence difference is positive in the region of the relative trough over western North America and negative in the relative ridge region over the North Pacific. Therefore, this result suggests that ageostrophic geopotential flux convergence plays a role in the lower level of the eddy kinetic energy in the region of the relative ridge and the higher level of the kinetic energy in the region of the relative trough in the control experiment.

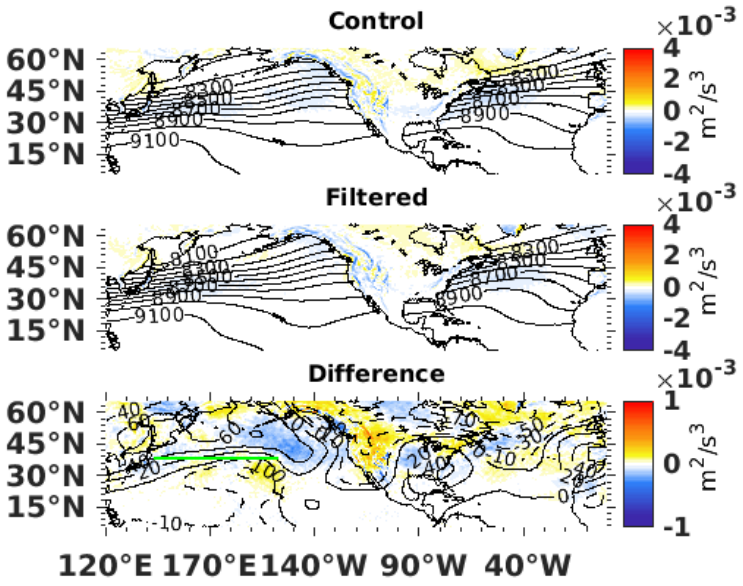

Figure 7. Geographical map of the mean ageostrophic geopotential flux convergence in the experiments. Shown are (color shades) $-\langle \nabla \cdot \boldsymbol{v}'\phi' \rangle$ and (contours) the mean geopotential height at 322 hPa for (top) the control experiment and (middle) the filtered experiment. Also shown are (bottom) the differences between the fields of the top two panels. The green line segment in the North Pacific along 38°N indicates the location of the vertical cross-sections of section 3.3.

While a convergence (positive) of the ageostrophic geopotential fluxes is the standard initiator mechanism of downstream baroclinic development in storm track dynamics [e.g., *Orlanski and Katzfey,* 1991; *Chang and Orlanski*, 1993], the fact that the mean intensity of the baroclinic energy conversion is not enhance in the relative trough regions, suggests that the enhance convergence of the ageostrophic geopotential fluxes in the presence of mesoscale SST anomalies (control experiment) does not lead to enhanced baroclinic energy conversion. Instead, we found it contributes to building the relative trough and the relative ridge to the west over the North Pacific.

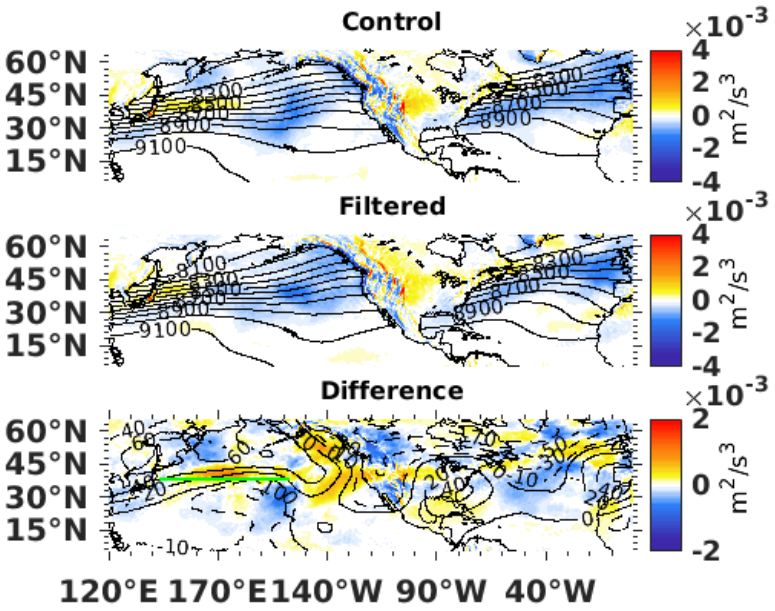

Figure 8. Geographical distribution of the barotropic eddy kinetic energy conversions in the experiments. Shown are (color shades) $-\overline{\langle \boldsymbol{v}' \cdot (\boldsymbol{v}'_3 \cdot \boldsymbol{\nabla}_3)\overline{\boldsymbol{v}} \rangle}$ and (contours) the time- and ensemble-average geopotential height at 322 hPa for (top) the control experiment and (middle) the filtered experiment. Also shown are (bottom) the differences between the fields of the top two panels. The green line segment in the North Pacific along 38°N indicates the location of the vertical cross-sections of section 3.3.

The next energetics process we investigate is barotropic energy conversion (Fig. 8). Off the coast of Japan, the barotropic energy conversion is positive in both experiments, indicating that kinetic energy is transferred from the time-mean flow to the eddies. Downstream of that region, along the storm track, barotropic energy conversion is negative in both experiments, indicating the kinetic energy is transferred from the eddies to the time-mean flow. This transfer is weaker in the control experiment, that is, the eddies lose less kinetic energy in the presence of mesoscale SST anomalies to the large-scale flow. The reduced transfer of kinetic energy to the large-scale flow is likely to play an important role in making the large-scale flow less zonal (building the relative ridge and trough in the control experiment) over the North Pacific storm track and western North America, as well as the eastern sector and the exit region of the North Atlantic storm track. Figure 9 shows the vertically-time average ensemble mean zonal wind

component, where the control experiment contains significantly less zonal wind throughout most of the North Pacific compared to the filtered experiment, indicating that SST mesoscale variability over the North Pacific plays a crucial role in the horizontal wind.

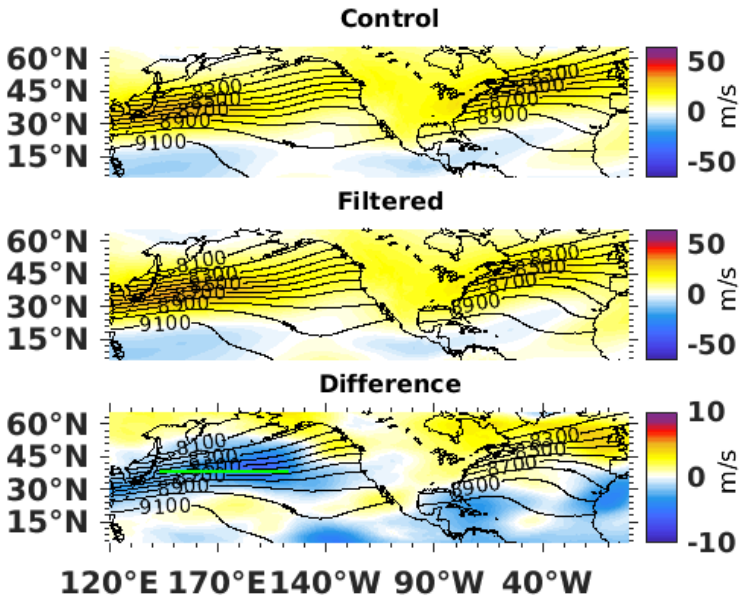

Figure 9. Geographical map of the vertical- time- ensemble-average zonal wind component (u) in the experiments. Shown are (color shades) u and (contours) the time- and ensemble-average geopotential height at 322 hPa for (top) the control experiment and (middle) the filtered experiment. Also shown are (bottom) the differences between the fields of the top two panels. The green line segment in the North Pacific along 38°N indicates the location of the vertical cross-sections of section 3.3.

Finally, we present the results for the residue term (Fig. 10). As expected, this term is dominantly negative in both experiments.

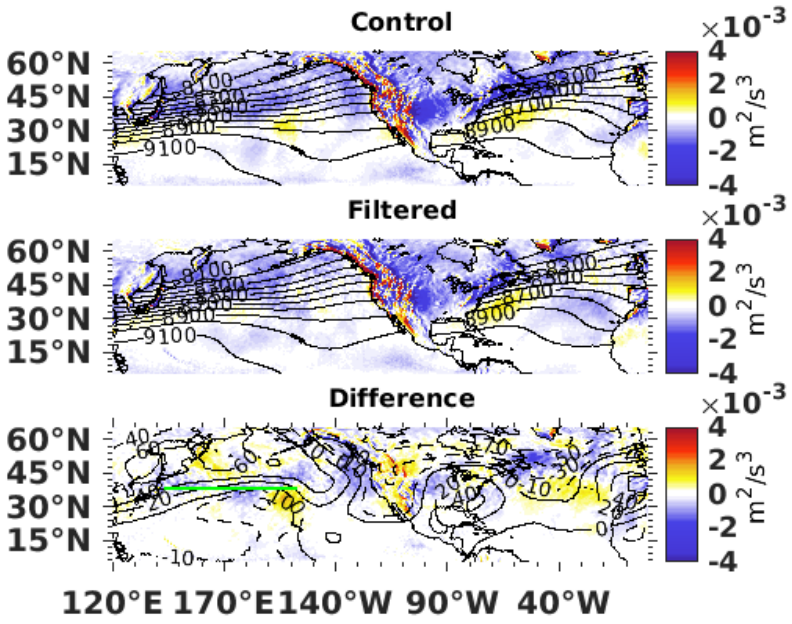

Figure 10. Geographical distribution of the eddy kinetic energy residual in the experiments. Shown are (color shades) the residual and (contours) the time- and ensemble-average geopotential height at 322 hPa for (top) the control experiment and (middle) the filtered experiment. Also shown are (bottom) the differences between the fields of the top two panels. The green line segment in the North Pacific along 38°N indicates the location of the vertical cross-sections of section 3.3.

3.4. Vertical Cross Sections of the Energetics

To further investigate the effects of the ocean mesoscale eddies of the Kuroshio Extension on the North Pacific storm track and jet, we prepare vertical cross sections of the different terms of the eddy kinetic energy equation along the latitude segment at 38°N that is marked by a green line segment in all the above figures with the exception of Figure 2. West of the dateline along this green line segment, the mesoscale SST anomalies associated with the ocean mesoscale eddies of the Kuroshio Extension have significant amplitudes. In fact, *Jia et al.* [2019] chose the same longitudinal segment to investigate the relationship between the SST anomalies associated with the ocean mesoscale eddies and atmospheric moisture. They concluded that the presence of ocean mesoscale eddies increased the atmospheric moisture

content by an enhancement of the vertical moisture fluxes in the lower troposphere. They reasoned that the enhanced baroclinic energy conversion may have been caused by the enhanced moisture fluxes. However, Figure 4 suggests that this is not the case. The vertical cross section of the baroclinic energy conversion (Fig. 11) shows that the reduction in the vertically integrated baroclinic energy conversion is caused by a mixture of reductions and enhancements at different latitudes and pressure levels, with reductions dominate east of 150°E in the mid-troposphere.

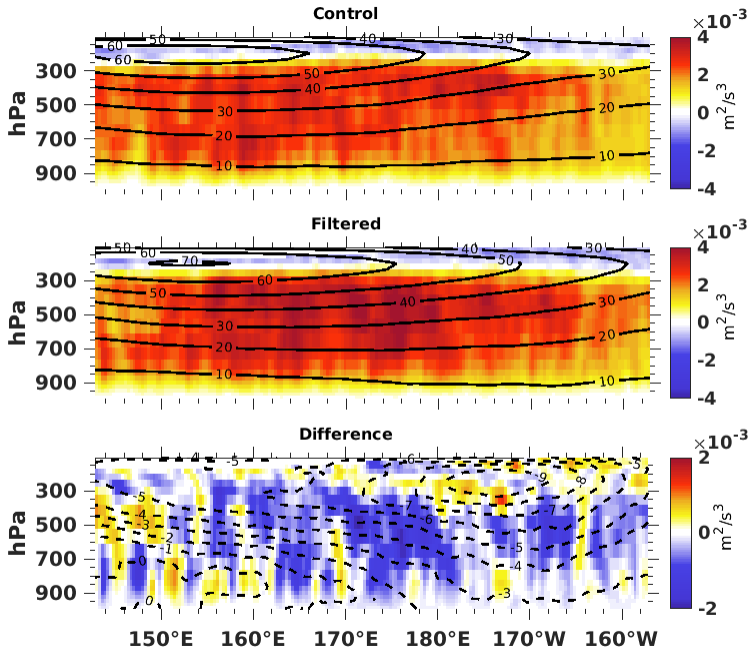

Figure 11. The effect of mesoscale SST variability on the baroclinic energy conversion along the Kuroshio Extension. Shown are the vertical cross sections of (color shades) $\overline{\omega'\alpha'}$ and (contours) the time- and ensemble-average zonal wind speed for (top) the control experiment and (middle) the filtered experiment. Also shown are (bottom) the differences between the fields of the top two panels.

In addition, the figure also shows that the zonal wind speed is reduced throughout the entire troposphere. Since the reduction of the zonal wind speed increases in magnitude with height, the vertical wind shear is also reduced except for the lowest atmospheric layer (below about 800 hPa) west of 175°E (Fig. 12), which helps explain the reduction in the intensity of the baroclinic energy conversion. The largest reduction in the zonal wind speed is found in the exit region of

the jet stream, effectively shortening the jet. Because baroclinic energy conversion is the result of baroclinic instability of the atmospheric flow and the strength of baroclinic stability is proportional to the vertical wind shear, the weakened wind shear must be an important part of the explanation of the reduced baroclinic energy conversion.

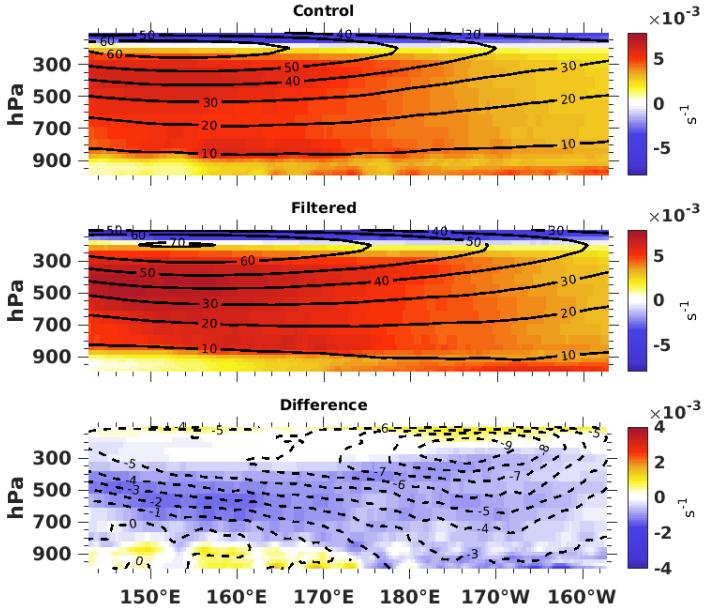

Figure 12. The effect of mesoscale SST variability on the vertical wind shear along the Kuroshio Extension. Shown are the vertical cross-sections of (color shades) the wind shear, $\overline{\partial u/\partial z}$ and (contours) the time- and ensemble-average zonal wind speed for (top) the control experiment and (middle) the filtered experiment. Also shown are (bottom) the differences between the fields of the top two panels.

One other important factor that affects baroclinic instability is the static stability of the atmospheric flow; where a weaker static stability leads to a stronger baroclinic instability. For a standard measure of the static stability, we create the vertical cross-section of the Brunt-Vaisala frequency (Fig. 13), which shows that the static stability is generally increased below the 700 hPa level, therefore contributes to the weakened baroclinic instability in the lowest atmospheric levels. While the static stability is reduced in the layer between 700 hPa and 300 hPa, the

reduced wind shear more than compensates the effect of the weakened static stability on the baroclinic instability of the atmospheric flow.

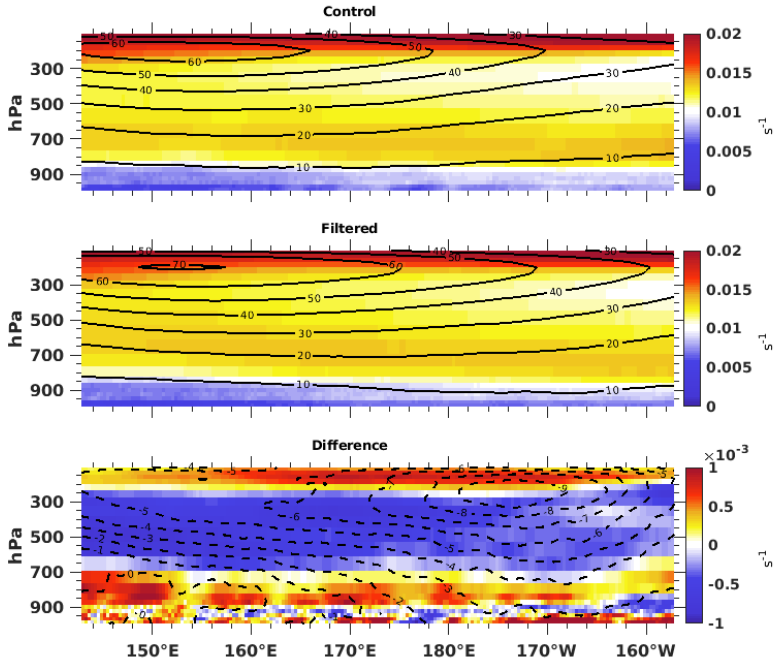

Figure 13. The effect of mesoscale SST variability on the static stability of the atmospheric flow along the Kuroshio Extension. Shown are the vertical cross-sections of (color shades) the Brunt-Vaisala frequency and (contours) the time- and ensemble-average zonal wind speed for (top) the control experiment and (middle) the filtered experiment. Also shown are (bottom) the differences between the fields of the top two panels. Note that a lower value of the Brunt-Vaisala frequency indicates weaker static stability.

This realization is also supported by the vertical cross-section of the daily growth rate of the most unstable mode of the Eady model of baroclinic instability (Fig. 14). The growth rate is defined by $e^{\sigma T}$, where

$$\sigma = 0.31 \frac{f}{N} \frac{\partial u}{\partial z} \tag{7}$$

and T = 24 h. Here in Equation 7, f = 10^{-4} is the typical value of the Coriolis parameter in the midlatitudes and N is the Brunt-Vaisala frequency. The parameter σ, which is often called the Eady-index, is the most frequently used measure of the baroclinic instability that combines the static stability and the vertical wind shear into a single measure. The figure shows that ocean

mesoscale eddies enhance the baroclinic instability only at the surface west of 170°E. East of 170°E, the baroclinic instability is greatly reduced at the surface. In addition, the baroclinic instability is also reduced in the layer between 800 hPa and 400 hPa.

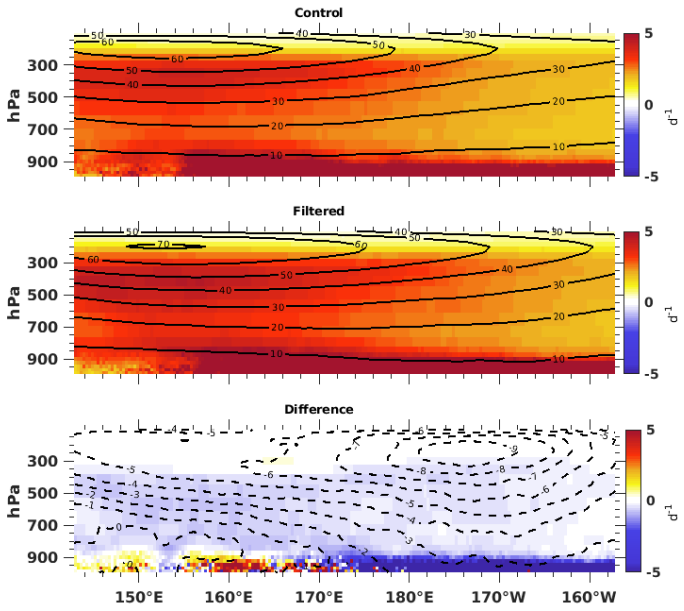

Figure 14. The effect of mesoscale SST variability on the baroclinic instability of the atmospheric flow along the Kuroshio Extension. Shown are the vertical cross-sections of (color shades) $\overline{\boldsymbol{e^{\sigma T}}}$ and (contours) the time- and ensemble-average zonal wind speed for (top) the control experiment and (middle) the filtered experiment. Also shown are (bottom) the differences between the fields of the top two panels.

Therefore, it is appropriate to ponder, what causes the weakening of the jet? Figure 15 offers an answer to this question, which represents the vertical cross section of the barotropic energy conversion. It is important to recall that the barotropic energy conversion is positive where kinetic energy is transferred from the mean flow to the atmospheric eddies and negative when kinetic energy is transferred from the atmospheric eddies to the mean flow. At the jet level, the barotropic energy conversion is positive west of the core of the jet and negative east of the core of the jet (top two panels of Fig. 15). In other words, the kinetic energy is transferred from the jet stream to the eddies west of the core of the jet and from the eddies to the jet east of the

core of the jet. Shown in the difference panel, we see that in the presence of SST mesoscale variability, the upstream positive transfer is enhanced, while the downstream negative transfer is suppressed. Overall, the net effect is a relative transfer of kinetic energy from the jet stream to the eddies in the jet layer, which explains the weaker jet illustrated in the control experiment.

Between the 600 hPa pressure level and the jet layer, the kinetic energy transfer is from the mean flow to the eddies. It is slightly weaker in the control experiment west of the dateline and positive elsewhere. In the lower and mid-troposphere east of the dateline, the kinetic energy transfer is from the eddies to the mean flow, but this transfer is weaker in the control experiment, resulting in a relative positive transfer of kinetic energy from the mean flow to the eddies in the presence of mesoscale SST variability.

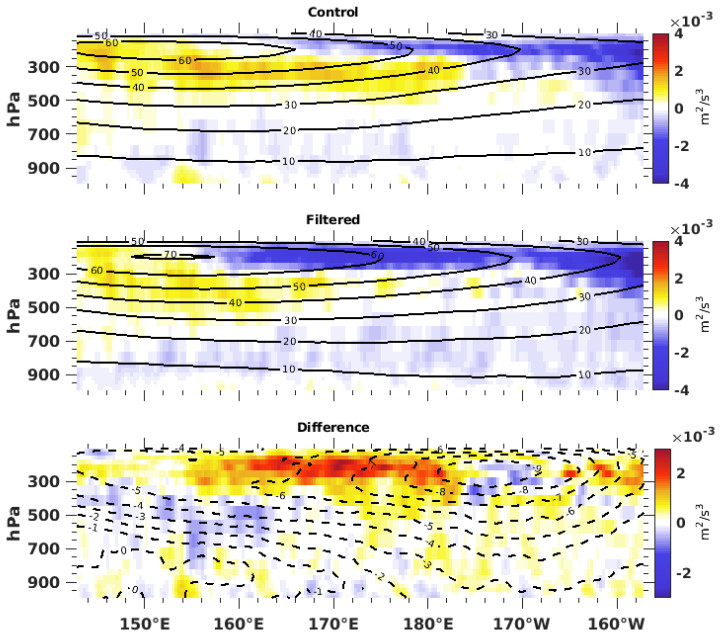

Figure 15. The effect of mesoscale SST variability on the barotropic energy conversion along the Kuroshio Extension. Shown are the vertical cross sections of (color shades) $\overline{\boldsymbol{\nu}' \cdot (\boldsymbol{\nu_3} \cdot \boldsymbol{\nabla_3})\overline{\boldsymbol{\nu}}}$ and (contours) the time- and ensemble-average zonal wind speed for (top) the control experiment and (middle) the filtered experiment. Also shown are (bottom) the differences between the fields of the top two panels.

Motivated by *Jia et al.* [2019], which found that the mesoscale ocean eddies of the Kuroshio Extension excited relative vertical motion, leading to enhanced vertical moisture and heat transport in the lower troposphere, we are also interested in the effect of these relative motions on the vertical eddy kinetic energy transport. The vertical eddy kinetic energy transport ranges from the lower troposphere (layer below 800-850 hPa) to the middle troposphere (Fig. 16). We can infer the effect of the ocean eddies on this transport by inspecting the differences (bottom panel of Fig. 16) in the lower troposphere: west of the dateline, where the magnitude of the SST anomalies are the greatest, there are both strong negative and positive differences near the surface of the ocean (below about 850 hPa), with the positive differences dominating. Investigating the next layer (between 850 hPa and 700 hPa) the differences are dominantly

negative, while in the layer above (between 700 hPa and 500 hPa) the differences are dominantly positive again. Therefore, this result suggests that the vertical motions excited by the ocean mesoscale eddies lead to a more efficient (negative) vertical transport of the eddy kinetic energy generated by baroclinic energy conversion in the layer between 850 hPa and 700 hPa.

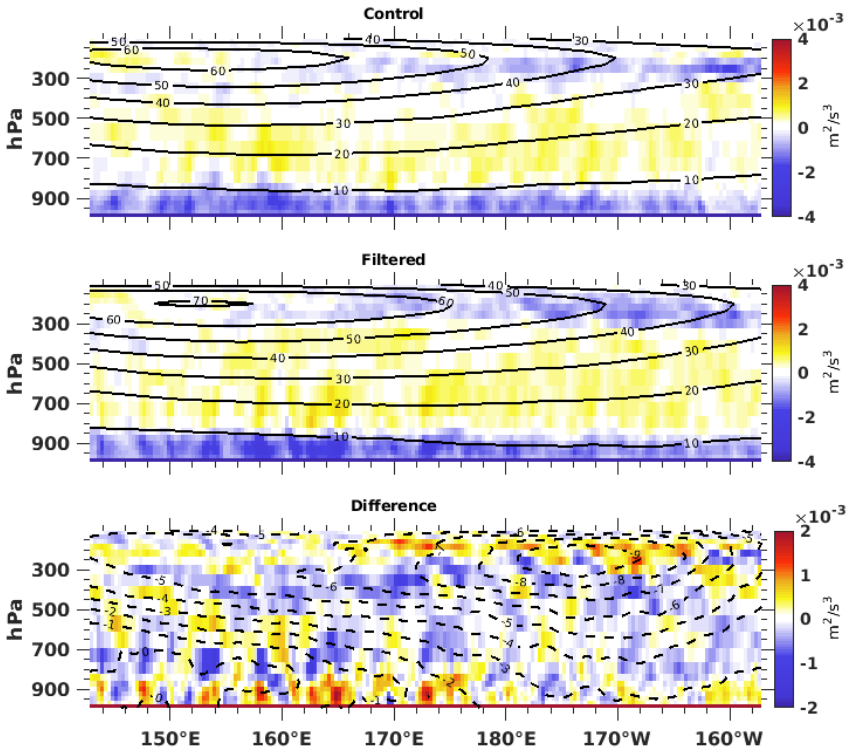

Figure 16. The effect of mesoscale SST variability on the vertical eddy kinetic energy transport along the Kuroshio Extension. Shown are the vertical cross sections of (colors shades) $-\overline{\nabla_p \cdot \boldsymbol{\omega}' \boldsymbol{K}_e}$ and (contours) the time- and ensemble-average zonal wind speed for (top) the control experiment and (middle) the filtered experiment. Also shown are (bottom) the differences between the fields of the top two panels.

Even though the differences fields associated with the different terms of the eddy kinetic energy equation are somewhat noisy, their net effect on the atmospheric eddy kinetic energy budget of the Kuroshio Extension region is extremely clear: the presence of mesoscale SST anomalies leads to a reduction of the eddy kinetic energy throughout the entire depth of the troposphere (Fig. 17).

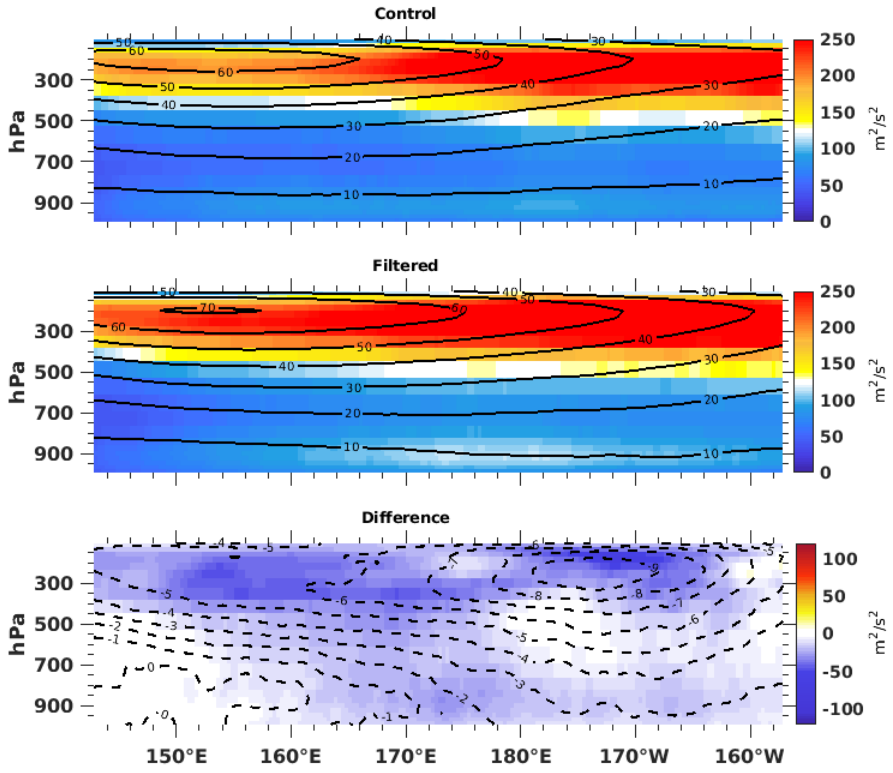

Figure 17. The effect of mesoscale SST variability on the eddy kinetic energy along the Kuroshio Extension. Shown are the vertical cross sections of (color shades) $\overline{\boldsymbol{E}}$ and (contours) the time- and ensemble-average zonal wind speed for (top) the control experiment and (middle) the filtered experiment. Also shown are (bottom) the differences between the fields of the top two panels.

4. CONCLUSIONS AND FUTURE WORK

4.1. Conclusions

We investigated the effects of ocean mesoscale SST variability on the midlatitude flow in the North Pacific. The investigation was built upon numerical experiments that were carried out with the NCAR CESM, using a configuration in which the atmospheric global circulation model was thermodynamically coupled to a slab ocean model. Using a resolution of 0.25°-by-0.25° that is sufficient to resolve a significant part of the mesoscale SST variability, that variability was only retained in one of the two ensembles (the control experiment). The effect of SST variability on the atmosphere was explored more in-depth by comparing the different terms of the atmospheric eddy kinetic energy equation for the two ensembles (control and filtered). Through our results it was found that mesoscale SST variability enhanced the upper tropospheric transfer of eddy kinetic energy from the core of the polar jet to the atmospheric eddies in the Kuroshio Extension region. The enhanced transfer of kinetic energy from the jet to the eddies weakened the core of the jet stream and led to a reduction of the vertical wind shear (baroclinic instability) of the time-mean flow. Furthermore, the production of eddy kinetic energy by baroclinic energy conversion was reduced. Therefore, the reduced generation of eddy kinetic energy in the Kuroshio Extension led to a downstream reduction of the kinetic energy that could be transferred from the atmospheric eddies to the North Pacific jet stream. The effect of mesoscale SST variability on the large-scale flow was similar to that of a drag force. In the exit region of the Pacific storm track, the effects of the changes of the upstream dynamics interacted with the larger scale atmospheric effects of the SST variability on the time-mean flow.

4.2. Future Work

We will expand the investigation to the North Atlantic. Investigating the North Atlantic will help us separate the general effects of mesoscale SST variability from those that are specific for the North Pacific.

REFERENCES

Chang, E. K. M., (1993). Downstream development of baroclinic waves as inferred from regression analysis. J. Atmos. Sci. 50, 2038–2053.

Chang, E. K. M., (2005). The impact of wave packets propagating across Asia on Pacific cyclone development. Mon. Wea. Rev. 133, 1998–2015.

Chang, E. K. M., and I. Orlanski (1993). On the dynamics of a storm track. J. Atmos. Sci. 50, 999–1015.

Chang, E. K., S. Lee, and K. L. Swanson, (2002): Storm track dynamics. J. Climate, 15, 2163-2183, https://doi.org/10.1175/1520-0442(2002)015<02163:STD>2.0.CO;2.

Chelton, D. B., and Xi., S. P., (2010). Coupled ocean-atmosphere interactions at oceanic mesoscales. Oceanography 23, 52–69.

Chelton, D. B., Schlax, M. G., Freilich, M. H., and Milliff, R. F., (2004). Satellite measurements reveal persistent small-scale features in ocean winds. Science 303, 978–983.

Dickson, R. R., and J. Namias, North American influences on the circulation and climate of the North Atlantic sector, Mon. Weather Rev., *104,* 728–744, 1976.

Foussard, A., Lapeyre, G., and Plougonven, R. (2019). Storm track response to oceanic eddies in idealized atmospheric simulations. J. Climate 32, 444–463.

Frankignoul, C., N. Sennechael, Y. –O. Kwon, and M. A. Alexander, (2011): Influence of the meridional shifts of the Kuroshio and the Oyashio Extensions on the atmospheric circulation. *J. Climate,* 24, 762-777, https://doi.org/10.1175/2010JCLI3731.1.

Herrera, M. A., I. Szunyogh, and J. Tribbia, 2015: Forecast uncertainty dynamics in the THORPEX Interactive Grand Global Ensemble (TIGGE). Mon. Wea. Rev., 144, 2739-2766, *https://doi.org/10.1175/MWR-D-15-0293.1*

Hoskins, B. J., and P. J. Valdes, On the existence of storm tracks, J. Atmos. Sci., 47, 1854–1864, 1990.

Jia, Y., Chang, P., Szunyogh, I., Saravanan, R., and Bacmeister, J. T. (2019). A modeling strategy for the investigation of the effect of mesoscale SST variability on atmospheric dynamics. Geophys. Res. Lett. 46, 3982–3989.

Levitus, S., (1982). Climatological Atlas of the World Ocean. NOAA Professional Paper 13, U.S. Government Printing Office, Washington D. C., 173 pp.

Ma, X., Chang, P., Saravanan, R., Montuoro, R.., Hsieh, J.-S., Wu, D., Lin, X, Wu, L., and Jing, Z. (2015). Distance influence of Kuroshio Eddies on North Pacific Weather Patterns. Scientific Report 5, 17785.

Ma, X., Chang, P., Saravanan, R., Montuoro, R.., Nakamura, D., Wu, D., Lin, X, Wu, L., and Jing, Z. (2017). Importance of resolving Kuroshio front and eddy influence in simulating North Pacific storm tracks J. Climate 30, 1861–1880.

Nakamura, H., Sampe, T., Tanimoto, Y., and Shimpo, A. (2004). Observed associa- tions among storm tracks, jet streams and midlatitude oceanic fronts. in Earth's Climate: The Ocean-Atmosphere Interaction, Eds. C. Wang, S. P. Xie, J. A. Carton, American Geophysical Union, 329–345.

Nakamura, H., Sampe, T., Goto, W., and Xie,, S.-P.. (2008). On the importance of midlatitude oceanic frontal zones for the mean state and dominant variability in the tropospheric circulation. Geophys. Res. Lett., 35, L15709.

O'Reilly, C. H., and A. Czaja, (2015): The response of the Pacific storm track and atmospheric circulation to Kuroshio Extension variability. Quart J. Roy. Meteor. Soc., 141, 52-66, https://doi.org/10.1002/qj.2334.

Orlanski, I., and Katzfey, J., (1991). Stages in the energetics of baroclinic systems. Tellus 47, 605–628.

Orlanski, I., Katzfey, J., and J. P. Sheldon (1995). The life cycle of a cyclone wave in the Southern Hemisphere. Part I: Eddy energy budget. J. Atmos. Sci., 48, 1972–1998.

Small, R. J., deSzoeke, S. P., Xie, S. P., O'Neill, L., Seo, H., Song, Q., Cornillon, P., Spall, M., Minobe S. (2008). Air-sea interaction over ocean fronts and eddies. Dynamics of Atmospheres and Oceans, 45, 274–319.

Szunyogh, I., 2014: Applicable Atmospheric Dynamics: Techniques for the Exploration of Atmospheric Dynamics. World Scientific. **http://www.worldscientific.com/worldscibooks/10.1142/8047**

Woollings, T., Hoskins, B., Blacjburn, M., Hassell, D., and Hodges, K. (2010). Storm track sensitivity to sea surface temperature resolution in a regional atmosphere model. Clim. Dyn., 35, 341–353.

Xie, S. P., (2004). Satellite observations of cool ocean-atmosphere interaction. Bull. Amer. Meteorol. Soc., 85, 274–319.